Continuous Hydrothermal Flow Synthesis of S-Functionalised Carbon Quantum Dots for Enhanced Oil Recovery

Ioan-Alexandru Baragau[a§], Zhen Lu[a§], Nicholas P. Power[b], David J. Morgan[c], James Bowen[d], Pedro Diaz[a*], and Suela Kellici[a*]

[a] School of Engineering, London South Bank University, 103 Borough Road, London, SE1 0AA, U.K. *E-mail: kellicis@lsbu.ac.uk, diazp@lsbu.ac.uk Web: www.nano2d.co.uk

[b] School of Life Health & Chemical Sciences, The Open University, Walton Hall, Milton Keynes, MK7 6AA, U.K.

[c] Cardiff Catalysis Institute, School of Chemistry, Cardiff University, Park Place, Cardiff, CF10 3AT, U.K.

[d] School of Engineering and Innovation, The Open University, Walton Hall, Milton Keynes, MK7 6AA, U.K.

§ Contributed equally to the paper

Abstract: Currently, there is a paucity in the exploration and application of carbon-based nanomaterials for enhanced oil recovery. Carbon quantum dots (CQDs), 0D materials consisting of a graphitic core covered by an amorphous carbon framework, were produced from glucose and *p*-sulfonic acid calix[4]arene (SCX4) *via* Continuous Hydrothermal Flow Synthesis (CHFS), an environmentally benign synthetic approach. The S-functionalised carbon quantum dots (S-CQDs) demonstrated excellent colloidal stability in aqueous and brine solutions, low retention on sand surface, and impressive enhanced oil recovery (EOR) of 17% at very low concentrations of 0.01 wt%. The mechanisms proposed for CQDs in increasing oil sweeping efficiency involves altering the carbonate rocks wettability towards water wet, and creating temporary log-jamming, where the ultra-small particle size (1.7 ± 0.7 nm) allows S-CQDs to recover oil trapped in tight reservoirs. The synthesised S-CQDs also demonstrate

photoluminescence, pH stability in the range of 3-11 and have excitation independent behaviour (300-360) with an emission peak at 433 nm.

Keywords: Carbon Dots, Continuous Hydrothermal Flow Synthesis, Glucose, Calixarenes, Biomass utilization, Enhanced Oil Recovery

1. Introduction:

The total accumulation of worldwide crude oil production to date is 263.4 billion barrels (bbl) as reported by OPEC [1]. However, there is an estimated 2,000 billion bbl of conventional (light) oil remaining in reservoirs worldwide according to the BP Statistic Review of World Energy 2019 [2]. Although enhanced oil recovery (EOR) methods can offer increase oil recovery of 10-20% [3] over water or gas injection recovery, there are limitations in terms of cost and environmental impact. For instance, surfactants mostly used in the chemical EOR field cases for carbonate reservoirs since 1975, are petroleum sulfonates, alkyl ether sulfate, and alkyl aryl sodium sulfonate etc., in concentrations of 1 to 4 wt% [4]. Thus, there's a need to explore more environmentally sustainable and economically viable methods for EOR.

Despite recent fast-paced development and diversity of new nanomaterials, relatively little exploration of their potential for EOR has been pursued as an alternative which offer possible benefits such as, efficient fluid displacement/sweep efficiency (due to small size and large surface area), low production cost, and a benign environmental impact [5–9]. The use of nanomaterials such as metal oxides (*e.g.* TiO_2, Al_2O_3, ZrO_2 etc.) and silicon dioxide in EOR have been widely investigated [5,9]. More recent but limited studies of carbon nanotubes, graphene, and carbon-based fluorescent dots [6–8] have demonstrated that carbon-based nanomaterials could improve oil sweeping efficiency via a number of different mechanisms: interfacial tension (IFT) reduction, which enhances oil-water emulsion formation to increase oil mobility; wettability alteration, changing the reservoir rock surface's wettability from oil-

wet to water-wet, hence allowing the oil to be readily detached from the rock surface; disjoining pressure, which enables nanofluid to spread on the rock surface; and log-jamming, temporarily blocking small porous throats by aggregation of nanoparticles and causing a pressure build up in adjacent porous throats, thus forcing out the trapped oil [9]. However, insufficient studies of carbon-based nanomaterials applications in EOR means a limited understanding of the mechanisms involved. Therefore, it is necessary to carefully study these novel materials, such as carbon quantum dots (CQDs), in their application for EOR.

CQDs classified as 0D material are on a fine border between molecules and materials, and have experienced significant interest in recent years [10–12]. CQDs typically consist of a graphitic core covered by an amorphous carbon framework, and a surface decorated with multiple functionalities, including polymers [10,13]. Their size, composition [14], and surface features are consequence of their synthetic process that is directly reflected in their final properties and characteristics as carbon quantum dots. Overall, CQDs tend to be photo- and chemically stable, biocompatible, and possess excellent optical properties [14]. In terms of the surface chemistry of the CQDs, the functional groups vary as the result of the carbon source, precursors, the pH of the synthetic environment, and the reaction conditions.

CQDs can be generated by the thermal degradation of any raw biomass sourced materials (*e.g.* coffee grounds, leaves, bird droppings) [15] but more usefully from biomass constituent molecules such as for example, glucose [16], fructose [17], cellulose [18], or citric acid [19], *i.e.* materials of known elemental provenance, in water and/or other polar solvents. By doping or functionalising the carbon quantum dots with elements such as nitrogen [20], sulfur [21], phosphorous [22], or other elements [23], the properties and characteristics of CQDs can be enhanced and tightly controlled compared to the pure CQDs. For instance, N-doped CQDs synthesised in our laboratory [19] exhibited excitation independent blue photoluminescence (PL), with a quantum yield of *ca.* 15%, and showed both, high selectivity and sensitivity for

chromium(VI) ions as a nano-sensor, in contrast the non-doped synthesised CQDs exhibited negligible PL. CQDs materials have also found applications in photocatalysis, energy storage, solar cells, bio-tagging, bio-imaging [24].

The synthetic methods for CQDs can be divided in two main categories: top-down (e.g. arc-discharge [25], laser ablation [26], and continuous laser-microfluidic vortex fluidic device [27]) where the starting carbon material is chemically or physically cut to achieve 20 nm or smaller particle size and bottom-up approaches, where raw materials are small molecules that form particles *via* inter- or intra-molecular dehydration, thermal decomposition or carbonization processes. Methods include microwave assisted [28], combustion/thermal routes [29], hydrothermal/solvothermal carbonization [14][30] and acidic oxidation [31].

Continuous Hydrothermal Flow Synthesis, CHFS, is one of the most promising hydrothermal methods for the bottom-up production of homogenous-quality inorganic nanomaterials [32–35] (homo/hetero metal oxide/s [36], metals [37,38], 2D derivatives [35,39–41], and carbon based [19]). The CHFS process involves mixing supercritical water with aqueous precursor feeds in rapid reaction times (milliseconds) with lower energy and time demands compared to traditional batch processes, providing high quality and reproducible homogenous products, with real-time full control over the reaction parameters. The application of CHFS to carbon nanomaterials synthesis was first reported for synthesis of reduced graphene oxide [41] and graphene quantum dots (GQDs) in our laboratory. GQDs were prepared from GO with tetraphosphonic acid calix[4]arene (PCX4) [42], and *p*-sulfonic acid calix[4]arene (SCX4) [43], where the macrocyclic molecules not only acted as stabilizers and/or size controllers, they also improved the GQD's optical properties, and significantly for the study herein, enhanced their solubility/dispersibility in aqueous solutions.

For CQDs synthesis [14,16], CHFS rivals batch-hydrothermal processes delivering significant advancements in material synthesis not only in independent control over reaction

parameters (*e.g.* temperature, pressure, and flow rates) and consequent particle properties, but also in that the process follows closely to Poliakoffs' 12 Principles of Green Engineering [44]. A life-cycle assessment study demonstrated that CHFS offers a simplified chemical process with improved efficiency and methodology that would reduce environmental impact for any potential scale-up for synthesis of carbon-related materials [42]. Applying CHFS to produce carbon-based materials from biomass constituent sources (*e.g.* glucose) provides a new direction in achieving large-scale production of homogenous high-quality nanomaterials, allowing for high demand production for EOR for crude oil production, for instance.

For the S-CQDs produced herein, glucose was the primary carbon source with *p*-sulfonic acid calix[4]arene (SCX4) serving as a functionalizing agent. Calixarenes are macrocyclic molecules consisting of phenolic units connected via methylene bridges into a cyclic vase-like structure maintained *via* intramolecularly hydrogen-bonded -OH groups on the lower rim. The upper rim of the macrocycle allows for functional groups, sulfonic acid in this instance of SCX4, which can provide 3D structured cavities, and/or charged/polar sites that can interact with either polar or nonpolar substrates, ions or molecules [43]. Herein the focus is the CQDs surfactant properties, in particular their application impact on oil-water interfacial tension reduction, wettability alteration, and log-jamming for EOR studies, with a clear emphasis on understanding the mechanisms for these applications. Furthermore, the PL properties of the CQDs, an indicator of the extent and diversity of functionality on the CQD surface, are also reported. Core flooding was conducted to investigate whether CQDs could provide high oil recovery in EOR using low nanomaterial concentrations. The stability of the CQDs in aqueous solution was studied by conducting experiments of CQDs aggregation in high salinity solutions and retention on sand surfaces.

2. Experimental Section:

2.1 Chemicals

All materials were purchased from commercial suppliers, unless otherwise stated, and used without further purification. Deionised water, 15 MΩ obtained from an ELGA Purelab system was used in all experiments. Anhydrous pure D-Glucose was purchased from Fisher Chemicals (U.K) and used as received. p-Sulfonic acid calix[4]arene (SCX4) was synthesized via adaptation of previously reported methods [45–47].

The crude oil used was from Expro North Sea Ltd (U.K.). It was diluted with heptane to have an API (American Petroleum Institute) gravity of 23° (915.9 kg/m^3) and dynamic viscosity of 72 cP (0.072 Pa s) at 25 °C. A 90,000 ppm NaCl solution was used as formation brine with a density of 1.087 g/mL. Indiana limestone cores with an absolute permeability and porosity of 214 mD (2.11×10^{-13} m^2) and 15% void volume, respectively, were purchased from Kocurek Industries INC., Hard Rock Division (USA). All cores were cleaned with toluene to remove crude oil, and acetone to remove NaCl, using a Soxhlet extraction, and were subsequently dried in an oven at 60 °C for 48 hrs before and after core flooding and centrifuge studies. Rock substrates for contact angle measurement were prepared from the same Indiana limestone cores and treated in crude oil, as stated earlier, at room temperature and atmospheric pressure for 60 days. The sand-pack was prepared with fine sand (grain size 150-210 μm) for measuring CQDs retention, where the sand-pack had a bulk volume (BV) of 75 mL, and pore volume (PV) of 24 mL.

2.2 Equipment

Freeze-drying was performed using a Heto PowderDry PL 3000.

X-Ray Photoelectron Spectroscopy (XPS): XPS measurements were performed using a Kratos Axis Ultra DLD photoelectron spectrometer utilizing monochromatic Al source

operating at 144 W (10 mA x 14 kV). Samples were mounted using conductive carbon tape placed on a glass slide to float them from the spectrometer and aid charge neutralisation, which was achieved using a flux of low energy electrons and a magnetic immersion lens. Survey and narrow scans were performed at constant pass energies of 160 and 40 eV, respectively and step sizes of 1 and 0.1 eV; the analysis area was approximately 700 x 300 μm^2. The base pressure of the system was ca. $1x10^{-9}$ Torr rising to ca. $4x10^{-9}$ Torr during analysis of these samples.

A High-Resolution Transmission Electron Microscope (HRTEM) JEOL JEM2100 equipped with LaB6 filament was used for particle size analysis. For the investigation, the acceleration voltage was set to 200 kV and the emission was set to 107 μA. The samples were prepared by depositing the aqueous solution of S-CQDs onto a holey carbon-coated Cu-grid. The particle size of CQDs was measured from TEM images using ImageJ software.

Fourier-Transform Infrared Spectroscopy (FT-IR): FT-IR spectra were recorded using a Nicolet Avatar 370DTGS spectrometer fitted with a Smart Orbit accessory (diamond 4000-200 cm^{-1}).

Raman Spectroscopy: The spectrum of the as-synthesised and dried CQDs was measured with a Renishaw Raman system using the 488 nm line of an Ar^+ ion laser at a power of ~10 mW.

Atomic Force Microscopy (AFM) imaging: CQDs were immobilised on single-side-polished p-type Si wafers (average roughness 77 pm). Each solution was diluted with HPLC grade H_2O (Fisher Scientific, UK) to 1% of its 'as received' concentration. For each CQDs type, a single 10 μL droplet was deposited on the Si wafer fragment and dried in an oven at 37 ^oC for 24 h. Upon visual inspection, a circular residue of solid material remained on the wafer. Upon AFM analysis, the outermost region of the circular residue was found to contain unaggregated CQDs at a surface density suitable for image acquisition.

Images of dimensions 2 μm × 2 μm were acquired using an Asylum Research MFP-3D AFM (Oxford Instruments, UK) operating in Intermittent Contact Mode at a temperature of 18 ^{o}C and a relative humidity of <40 %. Images were composed of 512 x 512 pixels and the scanning velocity was 2.5 μm/s. Rectangular pyramidal-tipped Si cantilevers (PPP-NCL, Windsor Scientific, UK) were employed; their nominal length, width, and tip diameter were 225 μm, 38 μm and <10 nm respectively. Images were analysed using Scanning Probe Image Processor software (Image Metrology, Denmark).

Steady-State Optical Characterisation**:** The material was optically characterized using absorption (UV-Vis spectrophotometry) and emission/excitation (photoluminescence spectrophotometry) techniques. The sample concentration (1.5 mg/mL) was determined by freeze-drying 10 mL of the purified carbon dot sample.

UV–Vis spectrophotometry: Adsorption measurements were conducted using a Shimadzu UV-1800, in the range of 200-700 nm in a 10 mm quartz cuvette.

Photoluminescence spectroscopy (PL): The fluorescence spectra were recorded with a Shimadzu RF-6000 Spectrofluorophotometer, in the range of 200-700 nm, using a 10 nm quartz cuvette.

Quantum Yield (QY) determination: QY value of the synthesized CQDs was calculated (Equation 1) by measuring the integrated PL intensity in aqueous dispersion of CQDs in comparison with the integrated PL of quinine sulfate in 0.1 M H_2SO_4 (standard) and it was plotted as integrated PL *vs* Absorbance (Figure S1) and from where the slopes (the gradient Δ) were extracted.

$$\theta_{CQDs} = \theta_S \cdot \frac{\Delta_{CQDs}}{\Delta_S} \cdot \left(\frac{\eta_{CQDs}}{\eta_S}\right)^2 \quad \text{Equation (1)}$$

Where:

θ_{CQDs} is the quantum yield of CQDs; θ_S is the quantum yield of standard (quinine sulfate 54%); Δ_{CQDs} is the slope of integrated PL of CQDs; Δ_S is the slope of integrated PL intensity of

the standard; η_{CQDs} is the refractive index of water (1.33); η_S is the refractive index of 0.1 M H_2SO_4 (1.33).

Zeta potential of carbon quantum dots was measured using a Particle Metrix Stabino®-NANOflex® System. The aqueous sample solution was added to a PTFE beaker fixed with an oscillating piston at the centre of the sample. The particles become immobilised between the beaker walls and piston and the oscillating piston created a fluid flow of mobile ions cloud around each particle. A streaming potential was consequently created and measured via in-situ electrodes. Running time for each sample was 60 seconds.

Images of oil pendant drop, oil bubble, and oil sessile drop were recorded using a goniometer/tensiometer comprising of a Leica Wild M3Z stereo microscope and a JVC TK-C1381 colour video camera. The shape of an oil drop/bubble was analysed by First Ten Angstroms Incorporated Drop Shape Analysis Software Version 2.0 to estimate the surface tension, interfacial tension (IFT), and contact angle.

Core flooding setup employed the following: three fluid accumulators which were filled with crude oil, brine, and CQDs nanofluid, accordingly; a Presearch Limited model 260D syringe pump with a Teledyne ISCO D-SERIES pump controller; and a Bronkhorst EL-PRESS pressure meter/digital controller to record the pressure during core flooding experiments. The oil production from core flooding experiments was measured using a Vinci video separator system which consists of a Sony FCB-EX980P camera, a 200 cm^3 burette with 120 cm^3 measurable volume, and 18 cm external diameter. The obtained measurements were analysed by using the Vinci Acquisition software. Each experiment was repeated three times, the mean value and standard deviation were reported. Prior to the core flooding experiments, the core sample was firstly fully immerged in 90,000 ppm brine in a beaker and was placed in a vacuum chamber. The vacuum was applied with a pump until there were no visible air bubbles escaping from the core sample; the core sample was then considered fully saturated with brine.

For EOR studies, a stock concentration of CQDs nanofluid (1.5 mg/ml) was diluted with 90,000 ppm NaCl solution to prepare a series of solutions with concentrations of 0.001 wt%, 0.005 wt% and 0.01 wt% in accordance to previous studies by Li *et al*. [48] and Luo *et al*. [8].

Wettability studies were evaluated via the U.S. Bureau of Mines (USBM) wettability index of core samples by measuring the water/oil displacement driven by the centrifugal force. This was determined by capillary pressure analysis during water-displacing oil (imbibition) and oil-displacing water (drainage) studies via a centrifuge method (VINCI Technologies refrigerated centrifuge model RC 4500). The capillary pressure was controlled by setting rotation speeds to increase from 1400 rpm to 3500 rpm according to a pre-test of the system. The selected parameter of 1400 rpm was the minimal rotation speed to exert pressure to have production, and 3500 rpm was the maximum rotation speed that avoids damaging the core samples studied. Data analysis was performed using CYDAREX CYDAR system.

Nanomaterial's retention on rock surfaces was measured using a KONTES 420830-1510 model Chromaflex glass column with 2.5 cm inner diameter and 15 cm length for sand-pack. Calibration curve method was employed using abovementioned UV-Vis spectrophotometry to determine CQDs concentration.

2.3 Continuous Hydrothermal Flow Synthesis (CHFS) of CQDs

Carbon quantum dots were produced using a continuous flow synthesis reactor, as previously reported [41–43]. The reaction system (Schematic 1), is constructed with 316SS Swagelok stainless steel fittings and tubing. It consists of a water heater, three Gilson 307 HPLC pumps that deliver the aqueous solution of precursors and supercritical water to the reaction zone; a post reactor cooler; and a back-pressure regulator (BPR) that maintains a constant pressure in the system. The flow rates used were 20:5:5 mL/min (P1:P2:P3) for Pump 1 (delivering DI water through heater), Pump 2 (pumping glucose, 70 mg/mL solution) and

pump 3 (delivering *p*-sulfonic acid calix[4]arene (SCX4), 5 mg/mL solution), respectively. In a typical experiment, SCX4 (5 mg/mL) was delivered via Pump 3 to meet a flow of a glucose (70 mg/mL) solution at a T-junction. The resulting mixture was then combined with superheated water (450 °C, 24.8 MPa) inside a counter-current mixer, whereupon the product formation occurred in a continuous mode. This was then followed by a cooling step, where the reaction mixture was passed through a vertical cooler and collected for further purification. Two samples of CQDs were prepared, one with (S-CQD) and one without (g-CQD) the presence of SCX4, all other conditions were kept the same.

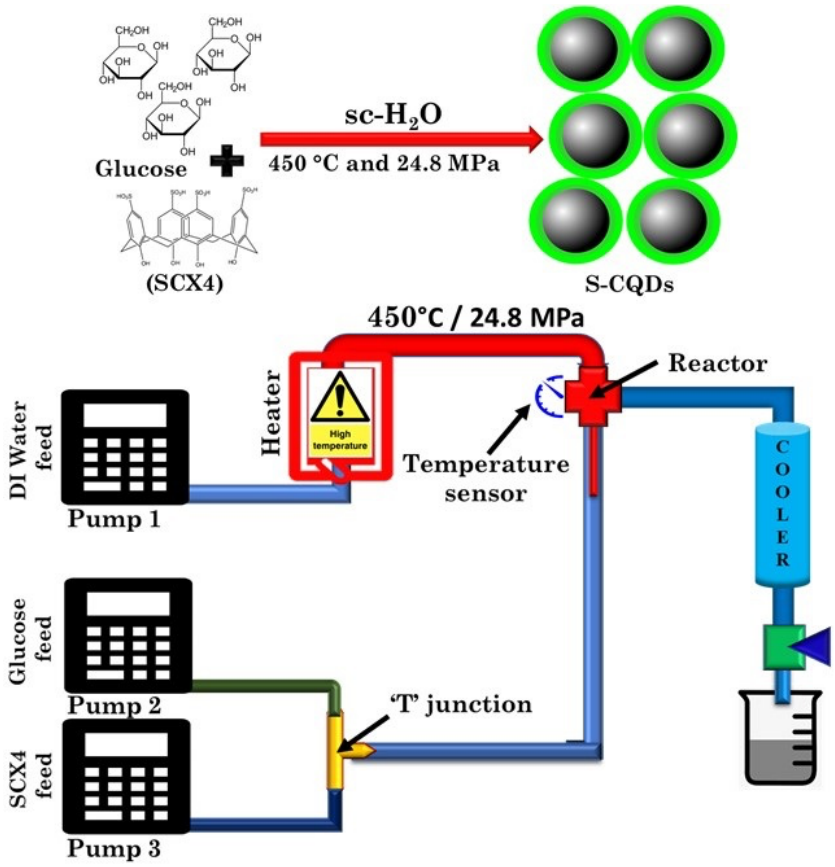

Schematic 1: Illustration of production process of S-carbon quantum dots (S-CQDs) using a Continuous Hydrothermal Flow Synthesis (CHFS) approach: (a) illustration of the CHFS synthesis process using glucose and *p*-sulfonic acid calix[4]arene (SCX4), (b) simplified CHFS design.

The purification process of the CHFS synthesized carbon quantum dots was divided into two steps: a) separation of the large particles according to size, and b) removal of small molecules by-products or/and precursors, followed by concentrating the materials to a stock volume. Initially, the larger particles were separated from the main solution via dead-end filtration through 0.2 µm pore size alumina membrane, followed by size separation *via* 30 kD membrane in a tangential filtration unit. The filtrate containing CQDs and other small molecules by-products and/or reaction precursors undergo further cleaning using a 1 kD membrane in a tangential filtration unit. The resulting solution is 20% of the initial volume and ready to be subjected to further experiments and analysis.

3. Results and Discussion:

3.1 Morphological and optical characterisations of carbon quantum dots.

The S-CQDs were analysed using steady-state optical characterisation **(**UV-Vis and photoluminescence spectrophotometry) to determine their optical & electronic properties, Raman and FT-IR spectroscopy to determine their functionalities, X-ray photoelectron spectroscopy (XPS) to determine the surface chemistry and elemental composition, High Resolution Transmission Electron Microscopy (HRTEM) and Atomic Force Microscopy (AFM) to ascertain the dimensions of the particles.

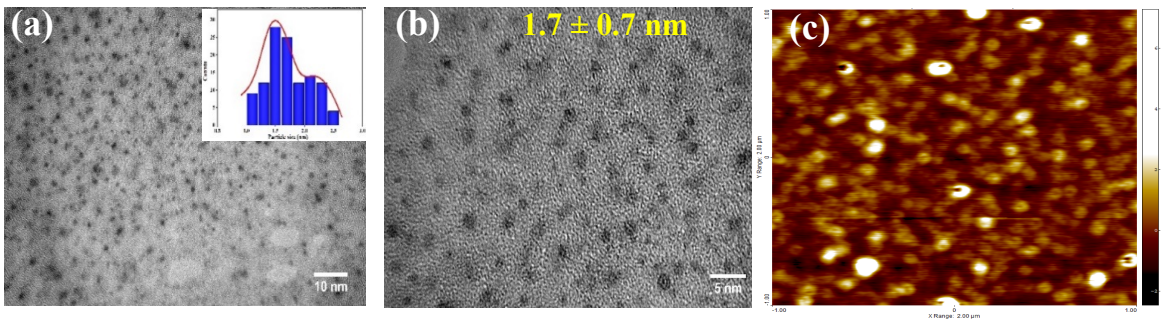

Figure 1: Morphological properties of S-CQD. (a-b) HR-TEM images of S-CQD at different scales and inset - particle size distribution histogram (c) AFM image.

Transmission Electron Microscopy (TEM) analysis showed round shaped morphology characteristic for CQDs with a mean particle size of 1.7 ± 0.7 nm, with a particle size range between 1.0 nm and 2.5 nm (**Figure 1a-b**), with sample homogeneity observed from the particle size distribution histogram to be predominantly between 1.5 nm and 2.0 nm.

The atomic force microscopy (AFM) image (**Figure 1c**) reveals the topography of the as-synthesised S-CQD with nanoparticles exhibiting mean diameter of 1.5 ± 1.1 nm (and maximum diameter 4.9 nm) and is complimentary with values determined from TEM. A minimum of 150 particles were analysed.

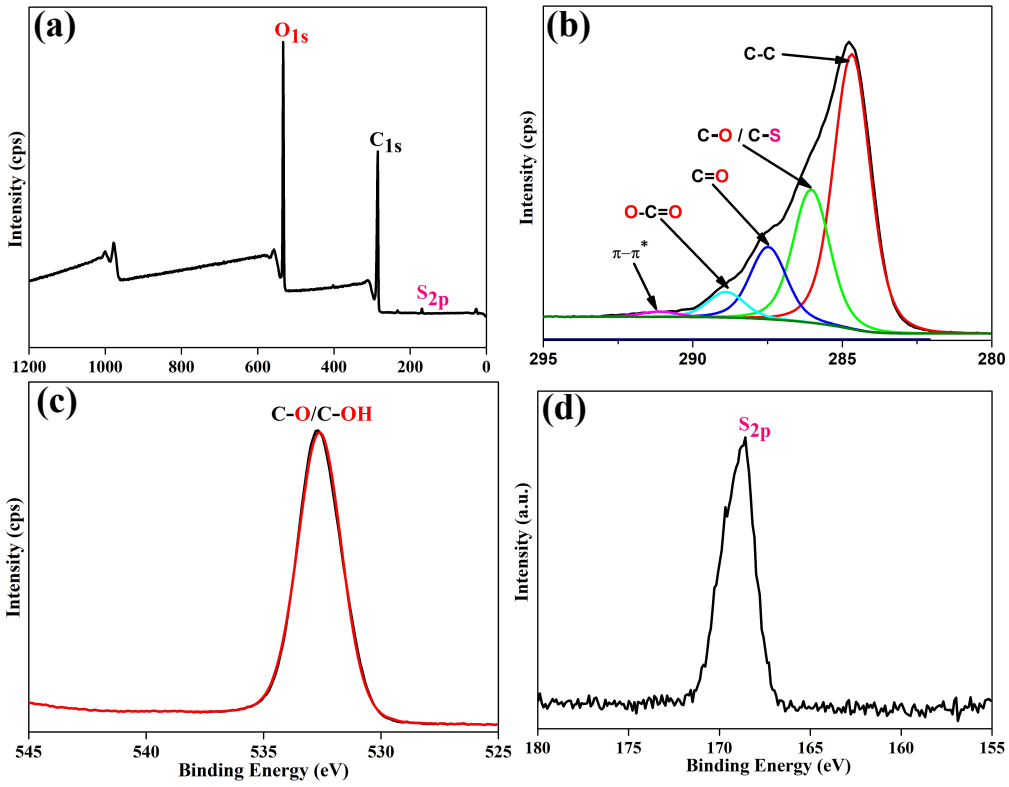

Figure 2: XPS survey scans of S-CQDs: (a) survey spectrum showing C(1s), S(2s) and O(1s) core levels, (b) fitted high-resolution spectra of C(1s), (c) O(1s) and (d) S(2p) regions.

X-ray photoelectron spectroscopy (XPS) studies (**Figure 2)** reveal the presence of the carbon, oxygen and sulfur atoms on the surface of the S-CQDs. In the expanded XPS spectra, the C1s peaks at 284.6 eV, 286 eV, 287.4 eV, 288.8 eV, and 291 eV can be assigned to C–C (sp^2), C–O/C-S (sp^3), C=O (sp^2), O–C=O (sp^2), and π-π* satellite respectively. The O(1s) peak has a maximum at 532.6 eV with an apparent asymmetry to lower binding energy. Due to the range of oxygen environments as inferred by the S(2p) and C(1s) core-level spectra, many of which will have similar binding energies, we have not attempted to fit this region and an $S(2p_{3/2})$ peak at 168.5 eV for C-SO_3H. The atomic ratio C/O is 2.27, and the CHFS as produced S-CQDs contain 30 at% oxygen, 1 at% sulfur and 69 at% carbon.

Raman spectroscopy confirms the presence of sp^2 carbon (graphitic core) in the S-CQDs sample as shown in **Figure 3a**, two broad peaks at 1385.8 and 1598 cm^{-1} correspond to the D and G bands, respectively. It is well known that the G band is attributed to an E_{2g} mode of graphite associated with the vibration of sp^2 bonded carbon atoms, indicating the aromatic character of the carbon dot's core; D band corresponds to sp^3 molecular defects [19].

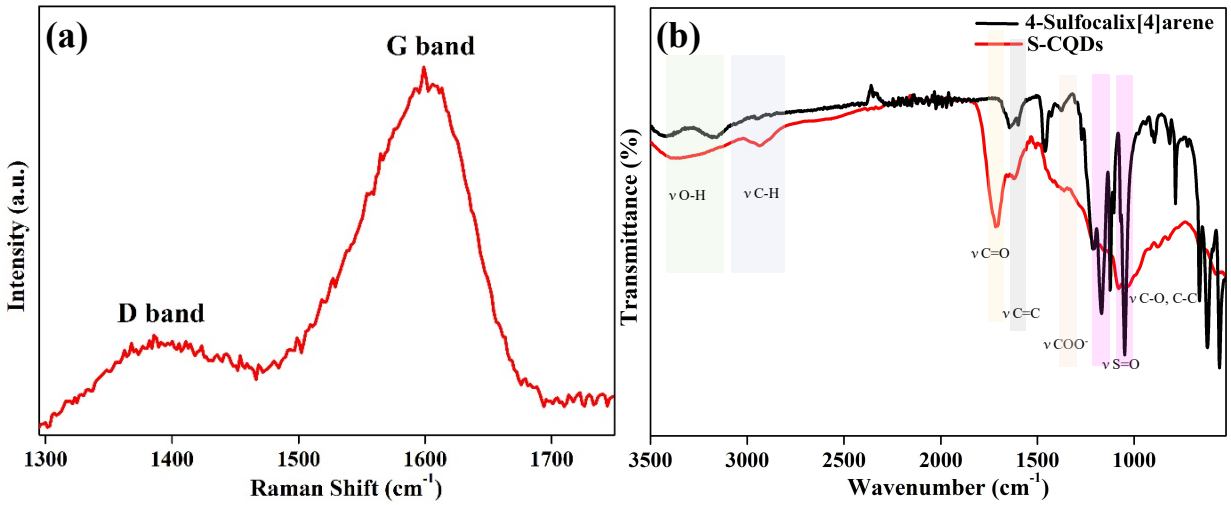

Figure 3: (a) Raman spectrum of S-CQDs, and (b) overlaid FTIR spectra of S-CQDs and SCX4.

The ratio of peak intensities of D and G bands, I_D/I_G for S-CQDs, which is indicative of disordered and aromatic domains, was determined as 0.7, revealing the graphitic core as the major component in the carbon dot's particle. The smaller D band peak is as a consequence of the oxygen content (30 at%) and presence of sp^3 carbon atoms, the results are in agreement with XPS data (see **Figure 2**).

The FT-IR spectroscopy (**Figure 3b**) lends further supports to the XPS and Raman analysis, indicating that S-CQDs exhibit a variety of oxygen functionalities (carbonyl, carboxyl or hydroxyl) on their surface. Also, this cocktail of oxygen functionalities lends excellent solubility in water of the S-carbon quantum dots. A broad peak (3500-2820 cm^{-1}) can be ascribed to the vibration of O-H (R-OH, -COOH), and C-H stretching vibrations (2931 cm^{-1}) for sp^3 hybridized carbon atoms. The carbonyl vibrations (for carboxyl, COO^-) could also be assigned for stretches at 1708 cm^{-1}, and C-O and C-O-C vibrations may be assigned to the stretch at 1045 cm^{-1}, respectively. The IR vibrations characteristic for S=O stretch (R-SO_3H) [43] for SCX4 are located at 1164 cm^{-1} and 1047 cm^{-1}; it's expected that these stretches would be significantly overlapped by carbon-oxygen functionalities of S-CQDs that absorb in the same domain given the low concentration of SCX4 used in synthesis (and is in agreement with XPS elemental analysis for S on the S-CQDs surface).

The UV-Vis spectrum (**Figure 4b)** displays two absorption bands centred at 225 nm and 278 nm with a tail extending in the visible region. The λ_{abs} = 225 nm band is generally assigned to the π–π* transitions of the aromatic C=C sp^2 domains typically found in the carbon dots graphitic core, whereas the λ_{abs} = 278 nm is due to the n–π* transitions of the functional groups located on the CQDs surface [49].Whilst irradiated by UV light, it was observed that the

transparent brown S-CQD solutions gave a light green luminescence, which was in contrast to the light blue for glucose CQDs (g-CQDs) previously reported [50].

The excitation independence (300 – 360 nm) observed can be assigned to surface state defects of the S-CQDs, a phenomenon previously reported for carbon based quantum dots (*e.g.* graphene oxide, doped carbon quantum dots) [19]. However, on excitation at longer wavelengths (380 nm to 440 nm) the emissions changed to excitation dependence, similar to the g-CQDs and also reported for lower energy excitation of the NCQDs [19], with emission maximum shifting from blue to green (503 nm to 530 nm), a feature that may be attributed to excitation for the π–π* transitions (for isolated sp^2 clusters) within the graphitic core.

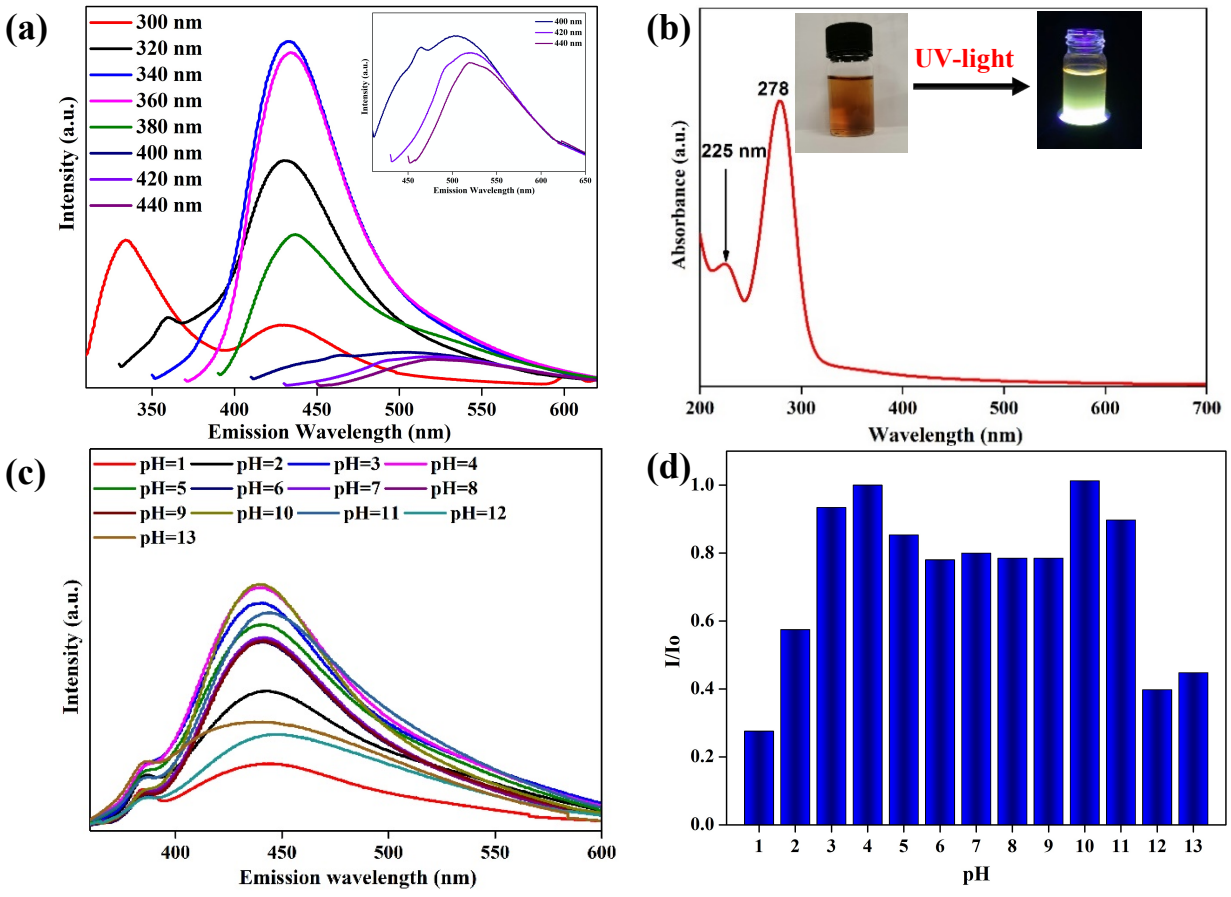

Figure 4: (a) Photoluminescence spectra at the different excitation wavelengths (b) UV-Vis spectrum with inset showing green PL when irradiated with UV-light at 365 nm (c) pH influence over the emission intensity (d) histogram of pH effect on the emission spectrum.

The pH-dependent behaviour of the S-CQDs can play an important role in their application in various systems; by varying the pH range between 1 and 13, the very nature of the S-CQDs surface structure can be modified as reflected by their emission performance, as explored in **Figure 4c - d**. The S-CQDs fluorescence demonstrated stability over a broad pH range (pH 3-11), although curiously optimal emissions were achieved at pH 4 and pH 10, but only ~ 80% of optimal emission intensity was achieved between pH 4 and pH 9. The lowest and highest pH values saw significant reduction (> 40 %) in emission intensity. The change in intensity is due to protonation and deprotonation of the various functionalities of the 0D structures surface (carboxylate, alcohol, sulfonate groups), thus disrupting the surface charge and its emissivity. The interesting behaviour observed between pH 3 and 11 may be attributed in part to the influence of SCX4 within the surface structure and the impact of intramolecular hydrogen bonding between its four phenolic protons (pK_1 = 3.26, pK_2 = 12.3, pK_3 = 12.9, pK_4 = 13.6) [51] and stabilisation between its varying anionic states. The quantum yield value of S-CQDs was measured to be 0.25% (calibrated against quinine sulfate in 0.1 M H_2SO_4 as standard), comparable to many literature reports for glucose derived CQDs [49].

3.2 EOR related characterisations.

In applying CQDs in enhanced oil recovery (EOR), their particle colloidal stability would be a very important factor to investigate, as any sedimentation or aggregation of the CQDs would be detrimental to their performance in EOR. To evaluate particle stability in solution, analysis of the materials zeta potential was undertaken; absolute zeta potential values for the particles greater than 30 mV would indicate they are typically stable [52]. The zeta potential of the S-CQDs was recorded as -42.3 mV for a particle concentration of 0.5 mg/ml. The zeta potential of the control sample CQDs (g-CQD) [50] was -25.8 mV for a concentration of 0.6 mg/ml, reflecting a lower stability compared to the S-CQDs. Solution of both CQDs sample

types (S-CQD and g-CQD) were prepared at concentrations of 0.01 wt% to determine their colloidal stability in both purely aqueous and high salinity systems (formation brine at 90,000 ppm).

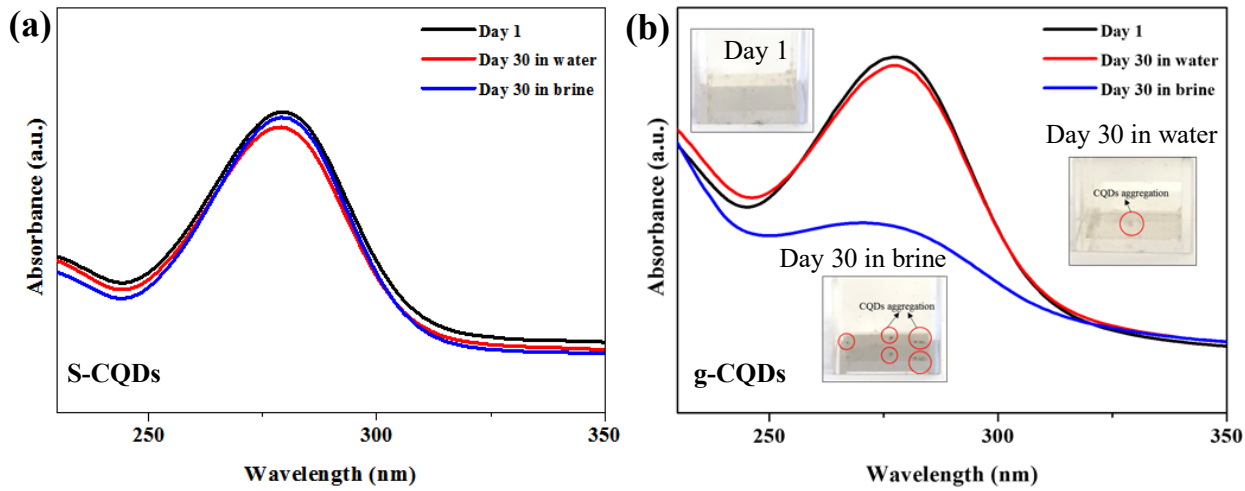

Figure 5: UV-Vis measurements, absorbance vs. time for stability study of (a) S-CQDs and (b) g-CQDs.

The solutions for each CQDs were stored at atmospheric pressure and 25 °C for 30 days and monitored by UV spectrophotometry to evaluate their degree of aggregation and deposition of the CQDs. UV-vis spectrum analysis for the water and brine dilutions of the CQDs nanofluids (**Figures 5**) displayed good colloidal water stability for both CQDs sample types. However, the g-CQDs brine sample, **Figure 5b**, revealed a significant reduction in UV absorbance reflecting aggregation/deposition of the particles from the solution. In contrast, the S-CQDs sample (**Figure 5a)** demonstrated excellent colloidal stability in brine.

Interfacial tension (IFT) between oil and water plays a very important role in oil recovery as water is the most common and convenient displacing medium [53] in the industry. The surface tension of S-CQDs nanofluid in air, and IFT of crude oil drop in S-CQDs brine nanofluid, were measured using pendant drop/raising bubble photographical method. The surface tension and IFT of g-CQDs sample and *p*-sulfonic acid calix[4]arene (SCX4) aqueous

solution were also measured for comparison. The concentration for all three samples were prepared at 0.01 wt%. The analysis of the results (**Figure 6)** showed no significant change for either the surface tension or IFT.

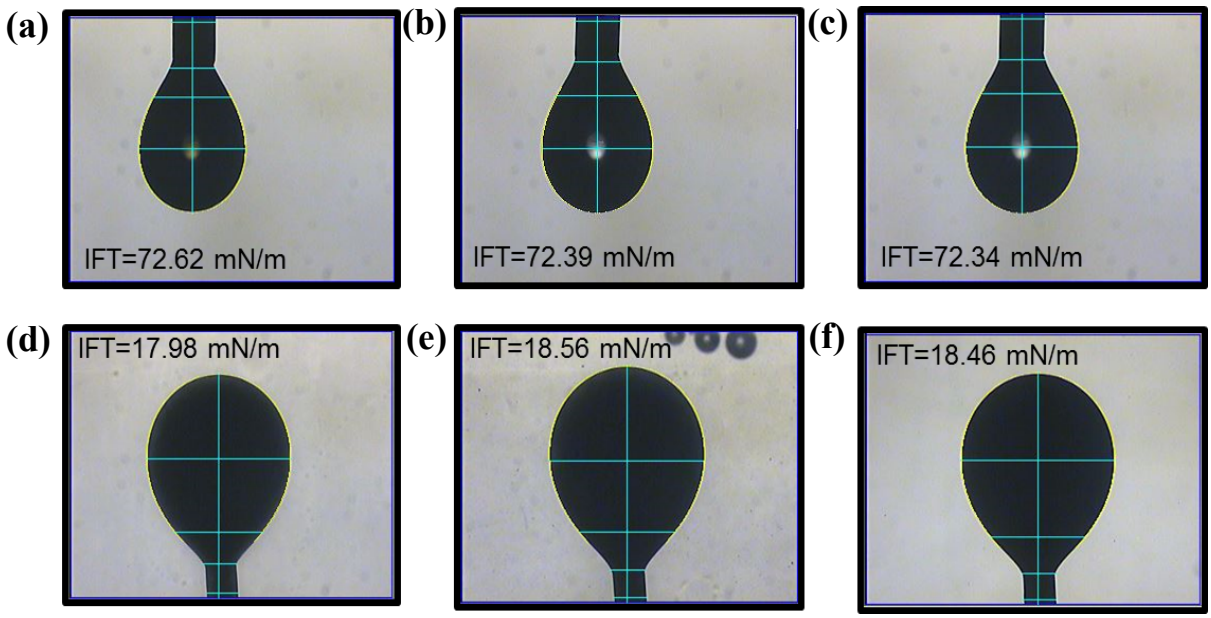

Figure 6: Pendant drops of nanofluid in air for (a) S-CQDs, (b) SCX4 aqueous solution, (c) g-CQDs. Oil bubbles in 90,000 ppm brine (d) S-CQDs, (e) SCX4, (f) g-CQDs.

In EOR, wettability plays a very important role, as water-wet rocks help improve water displacement of oil. The capillary driving force for water into a core's pores is stronger in a water-wet system. In this study, the wettability alteration was evaluated by contact angle measurement with oil sessile drop on a limestone substrate submerged in CQDs nanofluid (0.01 wt%).

From **Figure 7**, it can be observed that S-CQDs increased the contact angle of an oil drop on a limestone surface from 32.79º (in brine) to 49.78º, hence strongly indicating the limestone surface has been modified to be more water-wet, and that the oil is more detached from the limestone surface. The g-CQDs also significantly increased the oil drop contact angle (42.63º) on the limestone surface but to a lesser extent to that of the S-CQDs.

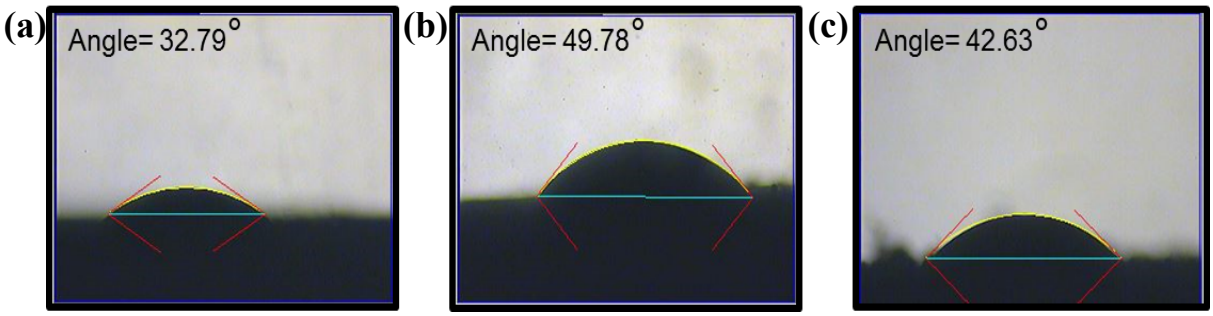

Figure 7: Crude oil sessile drop on limestone surface in surrounding liquid of (a) 90,000 ppm brine, (b) S-CQDs, and (c) g-CQDs.

The capillary pressure during water-displacing oil (imbibition) and oil- displacing water (drainage) processes was measured via the centrifuge method [54]. The wettability of the limestone core was measured before and after introducing S-CQDs into brine and three concentrations of the S-CQDs nanofluid (0.001 wt%, 0.005 wt%, and 0.01 wt%) were used.

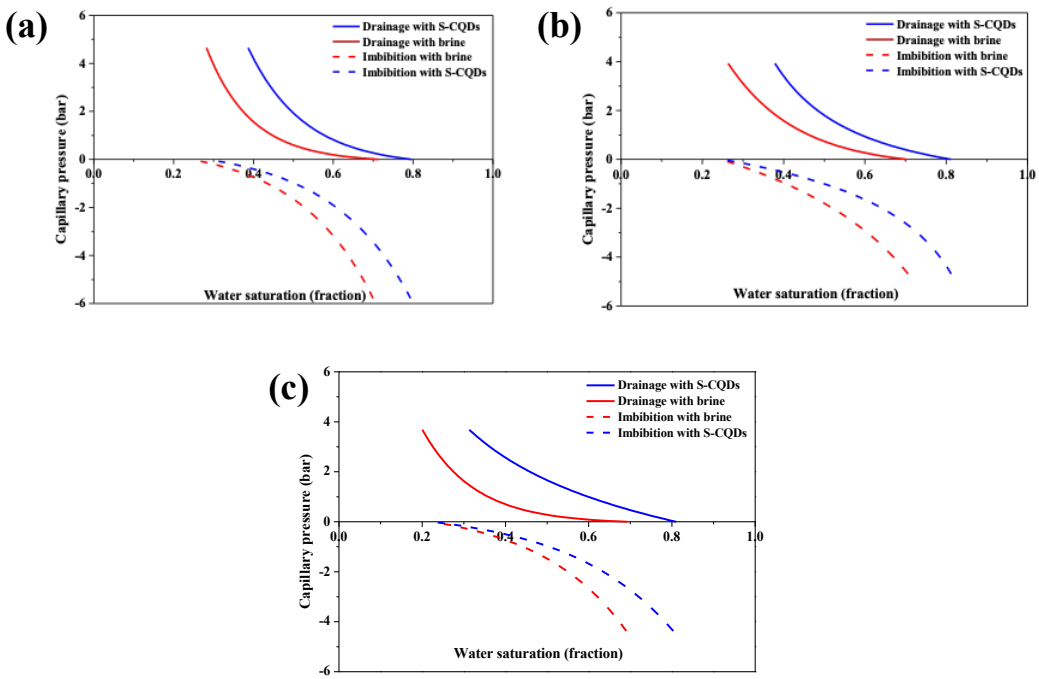

Figure 8: Drainage and imbibition curves with different concentration of S-CQDs (a) 0.001 wt%, (b) 0.005 wt%, and (c) 0.01 wt%.

The drainage and imbibition curves of the capillary pressure versus brine saturation were plotted (**Figure 8**) to calculate the U.S. Bureau of Mines (USBM) wettability index estimate [54]. The duration for one imbibition and drainage process was 14 days and thus considering the instability of g-CQD in brine, this test explores the properties of S-CQDs only which showed excellent colloidal stability in brine (**Figure 5**).

The USBM wettability index was determined from the ratio of log of the area under drainage curve and log of the area under imbibition curve. For the water wet system, the USBM index is greater than zero; but for an oil wet system, it is less than zero. The USBM index trend for increasing S-CQDs nanofluid concentration (**Figure 9**) shows that the wettability shifted from oil-wet to more water-wet with increasing concentration of S-CQDs.

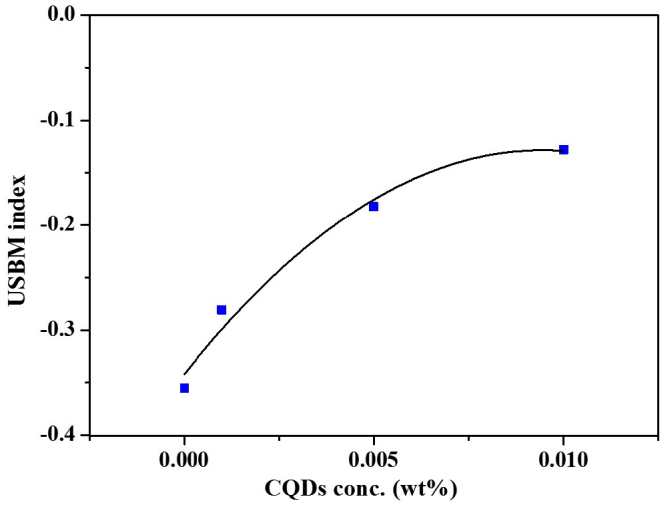

Figure 9: USBM index vs. S-CQDs concentration.

As it is mentioned before, the disjoining pressure enables nanofluid to spread on the rock surface. Wasan and Nikolov [55] stated that nanofluids tend to form thin wedges, and the wedges are driven by disjoining pressure. The disjoining pressure force associated with one single nanoparticle is small. However, a large amount of nanoparticles present can result in much larger disjoining pressure force, which is enough to drive the thin wedge film of nanofluids in the contact region of the oil sessile drop and rock surface. As a result, the oil

sessile drop is easier to be detached from the surface of rock. This reflects to a wettability alteration towards water-wet.

The core flooding test was used to measure incremental oil production driven by S-CQDs nanofluid. It is a process that simulates oil recovery from a reservoir. Typically, many of the dominant mechanisms such as wettability alteration and log-jamming are combined in this process, to recover oil from tight limestone under certain level of confining pressure (110 bar, 10 bar above oil injection pressure during drainage). Pressure drop versus oil production was recorded to determine the log-jamming mechanism.

In **Schematic 2**, three vertical cylinders (accumulators) were filled with S-CQDs nanofluid, brine, and crude oil, accordingly; the pump connected to the accumulators injected the fluids into the pre-saturated core sample. The core was placed in the core holder (110 bar, 25°C) and connected to the accumulators, the crude oil was injected at a rate of 1 ml/min through the core sample, using core flooding system for drainage process to create initial oil saturation [56]. Then, brine was injected (1 ml/min) for secondary oil recovery, followed by S-CQDs nanofluid at concentrations of (a) 0.001 wt%, (b) 0.005 wt%, and (c) 0.01 wt% for injection for EOR (1 ml/min). Low flow rate of 1 ml/min was chosen to optimise the length of core flooding experiments and to avoid high backpressure, front distortion and fingering. The production fluids were collected in a U-shape burette system for separation and volume measurement. The changing of oil-water interface was recorded for every minute, and the oil production was calculated from recorded images. From each test exercised there was an obvious pressure drop during S-CQDs nanofluid flooding, and a significant amount of oil was produced by the injection of S-CQDs nanofluid after the pressure drop occurred (**Figure 10**).

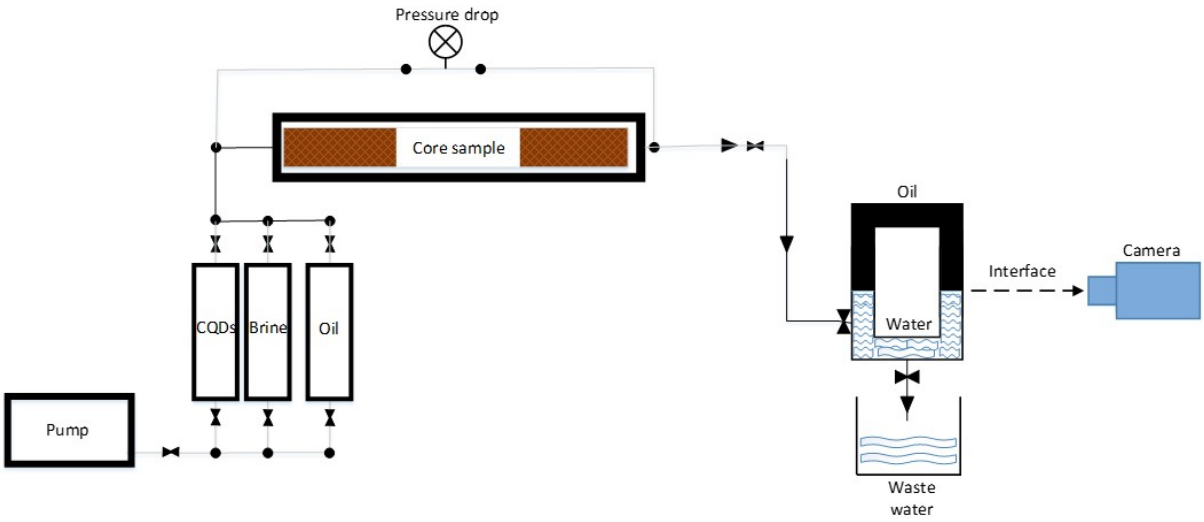

Schematic 2: Schematic of core flooding set-up

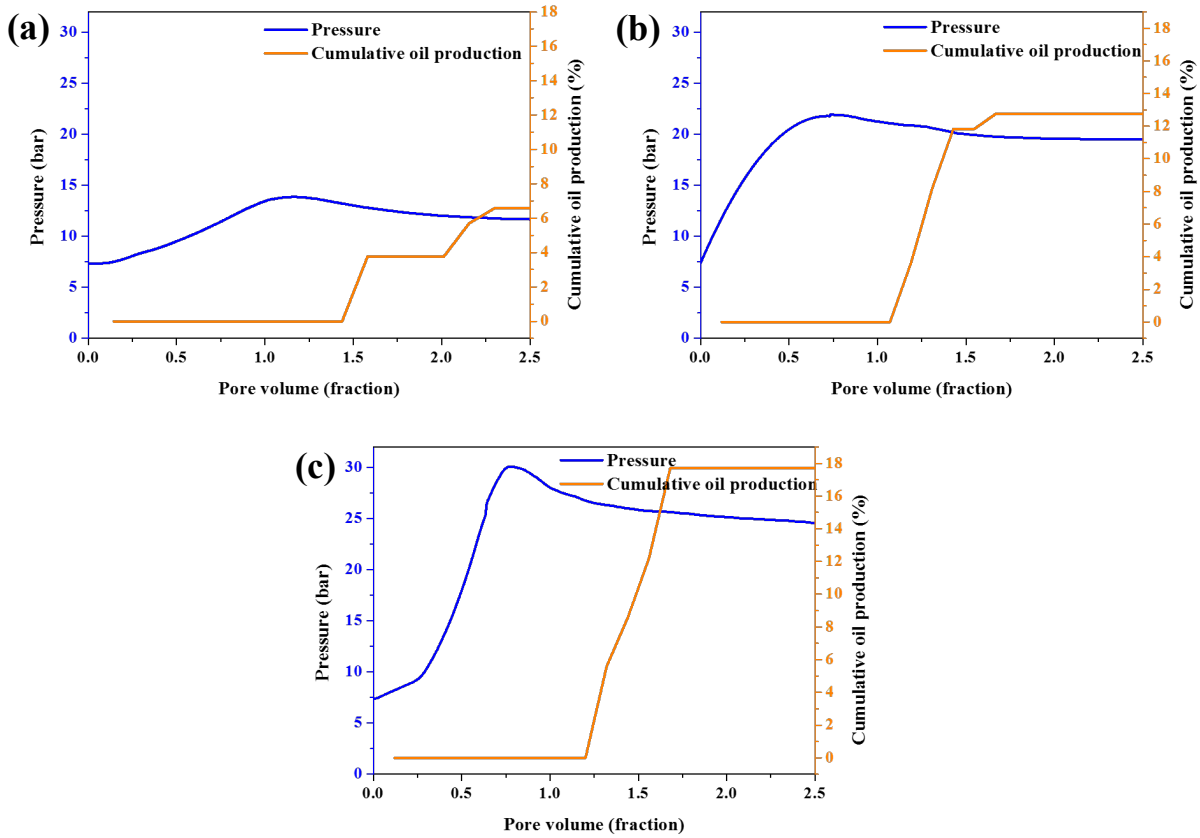

Figure 10: Cumulative oil production and pressure drop with different S-CQDs concentrations of (a) 0.001 wt%, (b) 0.005 wt%, and (c) 0.01 wt%.

The mechanism of this oil production can be explained by temporary *log-jamming*. Small sized particles tend to aggregate at the pores throats and block pathways, however, with continuous injection, the pressure on surrounding pores will build up due to this blockage, thus improving the sweeping efficiency. As more trapped oil is removed, the surrounding pressure decreases and the particle aggregates disassociate and disperse into the flooding fluid [57]. This can be associated to the observed pressure drop phenomenon in **Fig.10**. It can be seen in **Fig.10 (c)**, the pressure was first increased followed by a sharp decrease. The increasing of pressure can be explained by temporary blockage of pores throats by the S-CQDs aggregation. The higher the concentration of S-CQDs nanofluid, the quicker and easier it is to have the log-jamming to occur, thereby increasing the additional oil recovery factor incrementally by 7±0.1%, 13±0.2% and 17±0.2% respectively for S-CQDs nanofluid concentrations of 0.001 wt%, 0.005 wt% and 0.01 wt%. For comparison, core flooding with 0.01 wt% (optimum concentration) g-CQDs was also conducted. This gave an additional oil recovery of 15±0.5 %, whilst lower than that recorded for 0.01 wt% S-CQDs (possibly due to the lower colloidal stability and wettability alteration of the g-CQDs), the core flooding recovery obtained by using either material was higher than using conventional non-nano chemical surfactants or carbon derived NPs, as previously reported (**Table 1**) [58–60].

Table 1 Recovery factors using nanomaterials compared to that obtained using a surfactant.

Previously reported flooding material	**Flooding material concentration**	**Additional oil recovery factor**	**Ref.**
Cationic surfactant of dodecyltrimethylammonium bromide	4 wt%	19%	Firozjaii *et al.* [58]
Graphene-based nanosheets	0.01 wt%	15.2%	Luo *et al.* [59]
Sulfonated graphene	0.5 wt%	16%	Radnia *et al.* [60]

It can also be seen in **Table 1** that dodecyltrimethylammonium bromide achieved a higher oil recovery of 19%, but at a significantly higher surfactant concentration of 4 wt%, a four hundred fold difference in additive used. Both S-CQDs and g-CQDs proved to be more efficient and potentially, more economical.

The adsorption of the CQDs on to the rocks surface is a very important factor in EOR because it can alter the wettability and cause temporary *log-jamming*, however, if an overabundance of CQDs is adsorbed, it may reduce the oil recovery factor due to material loss and potential formation damage caused by blockage. S-CQDs had the best ability of enhancing oil recovery; therefore, the S-CQDs retention was measured to evaluate its adsorption on to the rock surface by the mass loss of S-CQDs from solution. A quarter of pore volume (PV) of a series of S-CQDs nanofluid dilutions (0.001 wt%, 0.005 wt% and 0.01 wt%) was injected into a sand-pack, and the S-CQDs concentration in the effluent was assessed by UV-Vis spectrophotometry.

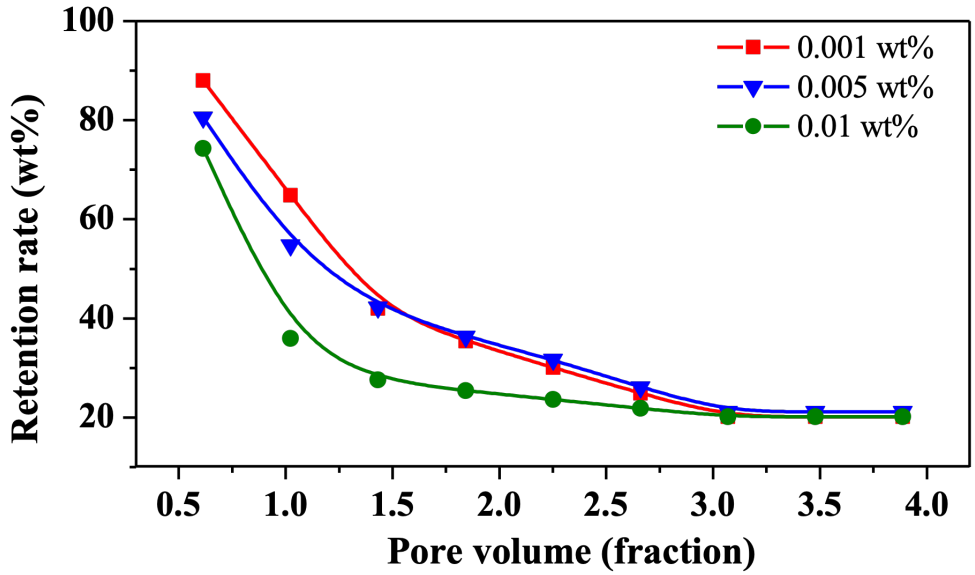

Figure 11: Retention rate vs. pore volume with different S-CQDs concentrations (wt%)

The S-CQDs retention rate was determined from the mass ratio of the recovered S-CQDs in the effluent to that of the total injected S-CQDs. The retention rate of S-CQDs was estimated to be ~ 20% with no significant change with increasing S-CQDs concentration (**Figure 11**).

4. Conclusions

In conclusion, a continuous hydrothermal flow synthesis route was developed for the production of carbon quantum dots starting from glucose as a biomass precursor and *p*-sulfonic acid calix[4]arenes as functionalising molecule. The photoluminescence studies for the S-CQDs exhibited an excitation independent behaviour (300-360 nm) with a maximum of emission peak at 433 nm and pH stability in the range 3-11. The CHFS produced S-CQDs and g-CQDs demonstrated excellent proficiency in providing high oil recovery of 17±0.2% and 15±0.5%, respectively using ultra-low concentrations of 0.01 wt%, which are more efficient and potentially economically beneficial than using other abovementioned nanoparticles. This can be attributed to their colloidal stability with the S-CQDs demonstrating greater stability over g-CQDs at high salinity conditions. The mechanisms proposed for S-CQDs in increasing oil sweeping efficiency involves altering rock wettability towards more water wet thus lowering retention on rock's surface, and creating temporary log-jamming, where the ultra-small particle size allows S-CQDs to recover oil trapped in tight reservoirs. There is scope to further explore S-CQDs potential in EOR, by increasing SCX4 doping levels for example, as well as exploiting their PL properties potential in various applications such as solar cells, sensing, photocatalysis, optoelectronics, biomedical and bio-tagging.

5. Conflict of interest

The authors have no conflicts of interest to declare.

6. Acknowledgements

SK, PD, IAB and ZL would like to acknowledge the financial support provided by LSBU. The authors would like to acknowledge the technical assistance of Dr Igor Kraev of the Open University Electron Microscopy Suite for HRTEM.

7. References:

[1] OPEC : World Proven Crude Oil Reserves: Cumulative production versus net additions, (2018). https://www.opec.org/opec_web/en/data_graphs/331.htm (accessed April 2, 2019).

[2] BP, BP Statistical Review of World Energy 2019, 2019.

[3] U.S.D. of Energy, Enhanced Oil Recovery _ Department of Energy, (2013). https://www.energy.gov/fe/science-innovation/oil-gas-research/enhanced-oil-recovery (accessed March 20, 2020).

[4] S. Pal, M. Mushtaq, F. Banat, A.M. Al Sumaiti, Review of surfactant-assisted chemical enhanced oil recovery for carbonate reservoirs: challenges and future perspectives, Pet. Sci. 15 (2018) 77–102. https://doi.org/10.1007/s12182-017-0198-6.

[5] H. Ehtesabi, M.M. Ahadian, V. Taghikhani, Enhanced Heavy Oil Recovery Using TiO2 Nanoparticles: Investigation of Deposition during Transport in Core Plug, Energy & Fuels. 29 (2015) 1–8. https://doi.org/10.1021/ef5015605.

[6] Y. Li, C. Dai, H. Zhou, X. Wang, W. Lv, Y. Wu, M. Zhao, A Novel Nanofluid Based on Fluorescent Carbon Nanoparticles for Enhanced Oil Recovery, Ind. Eng. Chem. Res. 56 (2017) 12464–12470. https://doi.org/10.1021/acs.iecr.7b03617.

[7] M. Shen, D.E. Resasco, Emulsions stabilized by carbon nanotube-silica nanohybrids, Langmuir. 25 (2009) 10843–10851. https://doi.org/10.1021/la901380b.

[8] D. Luo, F. Wang, J. Zhu, L. Tang, Z. Zhu, J. Bao, R.C. Willson, Z. Yang, Z. Ren,

Secondary Oil Recovery Using Graphene-Based Amphiphilic Janus Nanosheet Fluid at an Ultralow Concentration, Ind. Eng. Chem. Res. 56 (2017) 11125–11132. https://doi.org/10.1021/acs.iecr.7b02384.

[9] L. Hendraningrat, S. Li, O. Torsæter, A coreflood investigation of nanofluid enhanced oil recovery, J. Pet. Sci. Eng. 111 (2013) 128–138. https://doi.org/10.1016/J.PETROL.2013.07.003.

[10] M. Shamsipur, A. Barati, S. Karami, Long-wavelength, multicolor, and white-light emitting carbon-based dots: Achievements made, challenges remaining, and applications, Carbon N. Y. 124 (2017) 429–472. https://doi.org/10.1016/j.carbon.2017.08.072.

[11] S. Zhu, Q. Meng, L. Wang, J. Zhang, Y. Song, H. Jin, K. Zhang, H. Sun, H. Wang, B. Yang, Highly photoluminescent carbon dots for multicolor patterning, sensors, and bioimaging, Angew. Chemie - Int. Ed. 52 (2013) 3953–3957. https://doi.org/10.1002/anie.201300519.

[12] Y. Dong, H. Pang, H. Bin Yang, C. Guo, J. Shao, Y. Chi, C.M. Li, T. Yu, Carbon-based dots co-doped with nitrogen and sulfur for high quantum yield and excitation-independent emission, Angew. Chemie - Int. Ed. 52 (2013) 7800–7804. https://doi.org/10.1002/anie.201301114.

[13] P. Mirtchev, E.J. Henderson, N. Soheilnia, C.M. Yip, G.A. Ozin, Solution phase synthesis of carbon quantum dots as sensitizers for nanocrystalline TiO 2 solar cells, J. Mater. Chem. 22 (2012) 1265–1269. https://doi.org/10.1039/c1jm14112k.

[14] H. Luo, N. Papaioannou, E. Salvadori, M.M. Roessler, G. Ploenes, E.R.H. Eck, L.C. Tanase, J. Feng, Y. Sun, Y. Yang, M. Danaie, A. Belen Jorge, A. Sapelkin, J. Durrant, S.D. Dimitrov, M. Titirici, Cover Feature: Manipulating the Optical Properties of Carbon Dots by Fine-Tuning their Structural Features, ChemSusChem. 12 (2019) 4335–

4335. https://doi.org/10.1002/cssc.201902519.

[15] L. Wang, Z. Sofer, M. Pumera, Will Any Crap We Put into Graphene Increase Its Electrocatalytic Effect?, ACS Nano. 14 (2020) 21–25. https://doi.org/10.1021/acsnano.9b00184.

[16] N. Papaioannou, A. Marinovic, N. Yoshizawa, A.E. Goode, M. Fay, A. Khlobystov, M.M. Titirici, A. Sapelkin, Structure and solvents effects on the optical properties of sugar-derived carbon nanodots, Sci. Rep. 8 (2018) 1–10. https://doi.org/10.1038/s41598-018-25012-8.

[17] Y. Li, X. Zhong, A.E. Rider, S.A. Furman, K. Ostrikov, Fast, energy-efficient synthesis of luminescent carbon quantum dots, Green Chem. 16 (2014) 2566–2570. https://doi.org/10.1039/c3gc42562b.

[18] D.R. da Silva Souza, L.D. Caminhas, J.P. de Mesquita, F.V. Pereira, Luminescent carbon dots obtained from cellulose, Mater. Chem. Phys. 203 (2018) 148–155. https://doi.org/10.1016/j.matchemphys.2017.10.001.

[19] I.A. Baragau, N.P. Power, D.J. Morgan, T. Heil, R.A. Lobo, C.S. Roberts, M.M. Titirici, S. Dunn, S. Kellici, Continuous hydrothermal flow synthesis of blue-luminescent, excitation-independent nitrogen-doped carbon quantum dots as nanosensors, J. Mater. Chem. A. 8 (2020) 3270–3279. https://doi.org/10.1039/c9ta11781d.

[20] C. Yang, S. Zhu, Z.Z. Li, Z.Z. Li, C. Chen, L. Sun, W. Tang, R. Liu, Y. Sun, M. Yu, Nitrogen-doped carbon dots with excitation-independent long-wavelength emission produced by a room-temperature reaction, Chem. Commun. 52 (2016) 11912–11914. https://doi.org/10.1039/c6cc06673a.

[21] S. Chandra, P. Patra, S.H. Pathan, S. Roy, S. Mitra, A. Layek, R. Bhar, P. Pramanik, A. Goswami, Luminescent S-doped carbon dots: An emergent architecture for multimodal applications, J. Mater. Chem. B. 1 (2013) 2375–2382.

https://doi.org/10.1039/c3tb00583f.

[22] J. Zhou, X. Shan, J. Ma, Y. Gu, Z. Qian, J. Chen, H. Feng, Facile synthesis of P-doped carbon quantum dots with highly efficient photoluminescence, RSC Adv. 4 (2014) 5465–5468. https://doi.org/10.1039/c3ra45294h.

[23] J. Zhou, H. Zhou, J. Tang, S. Deng, F. Yan, W. Li, M. Qu, Carbon dots doped with heteroatoms for fluorescent bioimaging: a review, Microchimica Acta, 2017. https://doi.org/10.1007/s00604-016-2043-9.

[24] S.Y. Lim, W. Shen, Z. Gao, Carbon quantum dots and their applications, Chem. Soc. Rev. 44 (2015) 362–381. https://doi.org/10.1039/c4cs00269e.

[25] X. Xu, R. Ray, Y. Gu, H.J. Ploehn, L. Gearheart, K. Raker, W.A. Scrivens, Electrophoretic analysis and purification of fluorescent single-walled carbon nanotube fragments, J. Am. Chem. Soc. 126 (2004) 12736–12737. https://doi.org/10.1021/ja040082h.

[26] C.D. Buendia, R.T. Mendieta, A. Pyatenko, E. Falomir, M.F. Alonso, G.M. Vega, Fabrication by Laser Irradiation in a Continuous Flow Jet of Carbon Quantum Dots for Fluorescence Imaging, ACS Omega. 3 (2018) 2735–2742. https://doi.org/10.1021/acsomega.7b02082.

[27] X. Luo, A.H.M. Al-Antaki, K. Vimalanathan, J. Moffatt, K. Zheng, Y. Zou, J. Zou, X. Duan, R.N. Lamb, S. Wang, Q. Li, W. Zhang, C.L. Raston, Laser irradiated vortex fluidic mediated synthesis of luminescent carbon nanodots under continuous flow, React. Chem. Eng. 3 (2018) 164–170. https://doi.org/10.1039/c7re00197e.

[28] Z. Shen, C. Zhang, X. Yu, J. Li, Z. Wang, Z. Zhang, B. Liu, Microwave-assisted synthesis of cyclen functional carbon dots to construct a ratiometric fluorescent probe for tetracycline detection, J. Mater. Chem. C. 6 (2018) 9636–9641. https://doi.org/10.1039/C8TC02982B.

[29] J.J. Liu, D. Li, K. Zhang, M. Yang, H. Sun, B. Yang, One-Step Hydrothermal Synthesis of Nitrogen-Doped Conjugated Carbonized Polymer Dots with 31% Efficient Red Emission for In Vivo Imaging, Small. 14 (2018) 1–10. https://doi.org/10.1002/smll.201703919.

[30] A. Marinovic, L.S. Kiat, S. Dunn, M.-M.M. Titirici, J. Briscoe, Carbon-Nanodot Solar Cells from Renewable Precursors, ChemSusChem. 10 (2017) 1004–1013. https://doi.org/10.1002/cssc.201601741.

[31] P. Shen, Y. Xia, Synthesis-modification integration: One-step fabrication of boronic acid functionalized carbon dots for fluorescent blood sugar sensing, Anal. Chem. 86 (2014) 5323–5329. https://doi.org/10.1021/ac5001338.

[32] J.A. Darr, J. Zhang, N.M. Makwana, X. Weng, Continuous Hydrothermal Synthesis of Inorganic Nanoparticles: Applications and Future Directions, 2017. https://doi.org/10.1021/acs.chemrev.6b00417.

[33] P.W. Dunne, A.S. Munn, C.L. Starkey, T.A. Huddle, E.H. Lester, Continuous-flow hydrothermal synthesis for the production of inorganic nanomaterials, Philos. Trans. R. Soc. A Math. Phys. Eng. Sci. 373 (2015). https://doi.org/10.1098/rsta.2015.0015.

[34] Y. Hakuta, H. Hayashi, K. Arai, Fine particle formation using supercritical fluids, Curr. Opin. Solid State Mater. Sci. 7 (2003) 341–351. https://doi.org/10.1016/j.cossms.2003.12.005.

[35] U. Alli, S.J. Hettiarachchi, S. Kellici, Chemical Functionalisation of 2D Materials by Batch and Continuous Hydrothermal Flow Synthesis, Chem. - A Eur. J. 26 (2020) 6447–6460. https://doi.org/10.1002/chem.202000383.

[36] J.B.M. Goodall, S. Kellici, D. Illsley, R. Lines, J.C. Knowles, J. a Darr, Optical and photocatalytic behaviours of nanoparticles in the Ti-Zn-O binary system, RSC Adv. 4 (2014) 31799–31809. https://doi.org/10.1039/c3ra48030e.

[37] S. Kellici, J. Acord, A. Vaughn, N.P. Power, D.J. Morgan, T. Heil, S.P. Facq, G.I. Lampronti, Calixarene Assisted Rapid Synthesis of Silver-Graphene Nanocomposites with Enhanced Antibacterial Activity, ACS Appl. Mater. Interfaces. 8 (2016) 19038–19046. https://doi.org/10.1021/acsami.6b06052.

[38] G. Aksomaityte, M. Poliakoff, E. Lester, The production and formulation of silver nanoparticles using continuous hydrothermal synthesis, Chem. Eng. Sci. 85 (2013) 2–10. https://doi.org/10.1016/j.ces.2012.05.035.

[39] P.W. Dunne, A.S. Munn, C.L. Starkey, E.H. Lester, The sequential continuous-flow hydrothermal synthesis of molybdenum disulphide, Chem. Commun. 51 (2015) 4048–4050. https://doi.org/10.1039/c4cc10158h.

[40] V. Middelkoop, T. Slater, M. Florea, F. Neațu, S. Danaci, V. Onyenkeadi, K. Boonen, B. Saha, I.A. Baragau, S. Kellici, Next frontiers in cleaner synthesis: 3D printed graphene-supported CeZrLa mixed-oxide nanocatalyst for CO 2 utilisation and direct propylene carbonate production, J. Clean. Prod. 214 (2019) 606–614. https://doi.org/10.1016/j.jclepro.2018.12.274.

[41] S. Kellici, J. Acord, J. Ball, H.S. Reehal, D. Morgan, B. Saha, A single rapid route for the synthesis of reduced graphene oxide with antibacterial activities, RSC Adv. 4 (2014) 14858. https://doi.org/10.1039/c3ra47573e.

[42] S. Kellici, J. Acord, K.E. Moore, N.P. Power, V. Middelkoop, D.J. Morgan, T. Heil, P. Coppo, I.A. Baragau, C.L. Raston, Continuous hydrothermal flow synthesis of graphene quantum dots, React. Chem. Eng. 3 (2018) 949–958. https://doi.org/10.1039/c8re00158h.

[43] S. Kellici, J. Acord, N.P. Power, D.J. Morgan, P. Coppo, T. Heil, B. Saha, Rapid synthesis of graphene quantum dots using a continuous hydrothermal flow synthesis approach, RSC Adv. 7 (2017) 14716–14720. https://doi.org/10.1039/c7ra00127d.

[44] S.Y. Tang, R.A. Bourne, R.L. Smith, M. Poliakoff, The 24 Principles of Green Engineering and Green Chemistry: “IMPROVEMENTS PRODUCTIVELY,” Green Chem. 10 (2008) 268. https://doi.org/10.1039/b719469m.

[45] C.D. Gutsche, D. Dhawan, M. Leonis, D. Stewart, p-tert-BUTYLCALIX[6]ARENE, Org. Synth. 68 (1990) 238. https://doi.org/10.15227/orgsyn.068.0238.

[46] R. Lamartine, J.B. Regnouf de Vains, P. Choquard, A. Marcillac, Process for the dealkylating sulfonation of p-alkyl calixarenes, US Patent No: 5,952,526 (US005952526A), 1999.

[47] S. Shinkai, K. Araki, T. Tsubaki, T. Arimura, O. Manabe, New syntheses of calixarene-p-sulphonates and p-nitrocalixarenes, J. Chem. Soc. Perkin Trans. 1. 1 (1987) 2297–2299. https://doi.org/10.1039/p19870002297.

[48] S. Li, M. Genys, K. Wang, O. Torsæter, Experimental study of wettability alteration during nanofluid enhanced oil recovery process and its effect on oil recovery, in: Soc. Pet. Eng. - SPE Reserv. Characterisation Simul. Conf. Exhib. RCSC 2015, Society of Petroleum Engineers, 2015: pp. 393–403. https://doi.org/10.2118/175610-ms.

[49] S. Zhu, Y. Song, X. Zhao, J. Shao, J. Zhang, B. Yang, The photoluminescence mechanism in carbon dots (graphene quantum dots, carbon nanodots, and polymer dots): current state and future perspective, Nano Res. (2015). https://doi.org/10.1007/s12274-014-0644-3.

[50] I.A. Baragau, N.P. Power, D.J. Morgan, T. Heil, R.A. Lobo, C.S. Roberts, M. Titirici, S. Dunn, S. Kellici, Continuous hydrothermal flow synthesis of carbon quantum dots using a targeted biomass precursor for metal ions nano-sensing, Submitted. (2020).

[51] C.D. Gutsche, Calixarenes - an introduction, 2008. https://doi.org/10.1039/9781847558190.

[52] C. Freitas, R.H. Müller, Effect of light and temperature on zeta potential and physical

stability in solid lipid nanoparticle (SLN®) dispersions, Int. J. Pharm. 168 (1998) 221–229. https://doi.org/10.1016/S0378-5173(98)00092-1.

[53] B. Royce, E. Kaplan, M. Garrell, T.M. Geffen, Enhanced oil recovery water requirements, Miner. Environ. 6 (1984) 44–53. https://doi.org/10.1007/BF02072654.

[54] E.C. Donaldson, R.D. Thomas, P.B. Lorenz, Wettability Determination and Its Effect on Recovery Efficiency, Soc. Pet. Eng. J. 9 (1969) 13–20. https://doi.org/10.2118/2338-pa.

[55] D.T. Wasan, A.D. Nikolov, Spreading of nanofluids on solids, Nature. 423 (2003) 156–159. https://doi.org/10.1038/nature01591.

[56] S. Kiani, M.M. Zadeh, S. Khodabakhshi, A. Rashidi, J. Moghadasi, Newly Prepared Nano Gamma Alumina and Its Application in Enhanced Oil Recovery: An Approach to Low-Salinity Waterflooding, Energy and Fuels. 30 (2016) 3791–3797. https://doi.org/10.1021/acs.energyfuels.5b03008.

[57] A. Bila, J.Å. Stensen, O. Torsæter, Experimental investigation of polymer-coated silica nanoparticles for enhanced oil recovery, Nanomaterials. 9 (2019) 1–25. https://doi.org/10.3390/nano9060822.

[58] A.M. Firozjaii, A. Derakhshan, S.R. Shadizadeh, An investigation into surfactant flooding and alkaline-surfactant-polymer flooding for enhancing oil recovery from carbonate reservoirs: Experimental study and simulation, Energy Sources. 40 (2018) 2974–2985. https://doi.org/10.1080/15567036.2018.1514439.

[59] D. Luo, F. Wang, J. Zhu, F. Cao, Y. Liu, X. Li, R.C. Willson, Z. Yang, C. Chu, Z. Ren, Nanofluid of graphene-based amphiphilic Janus nanosheets for tertiary or enhanced oil recovery: High performance at low concentration, Proc. Natl. Acad. Sci. 113 (2016) 7711–7716. https://doi.org/10.1073/pnas.1608135113.

[60] H. Radnia, A. Rashidi, A.R. Solaimany Nazar, M.M. Eskandari, M. Jalilian, A novel

nanofluid based on sulfonated graphene for enhanced oil recovery, J. Mol. Liq. 271 (2018) 795–806. https://doi.org/10.1016/j.molliq.2018.09.070.